

Article

Grain Boundary Migration as a Self-Healing Mechanism of Tungsten at High Temperature

Ruxin Zheng¹, Liuqing Yang¹ and Liang Zhang^{1,2,*} 

¹ International Joint Laboratory for Light Alloys (MOE), College of Materials Science and Engineering, Chongqing University, Chongqing 400044, China

² Shenyang National Laboratory for Materials Science, Chongqing University, Chongqing 400044, China

* Correspondence: liangz@cqu.edu.cn

Abstract: The tungsten components in nuclear fusion reactors need to withstand the radiation cascade damage caused by the neutron bombardment of high temperature and high throughput fusion reaction during service. These damages are mainly present as a high concentration of point defects and clusters, which lead to a series of problems such as irradiation-hardening and decreased thermal conductivity of materials. In this study, molecular dynamics simulations are carried out to study the dynamic interaction between grain boundaries and the void in tungsten at high temperatures ($T > 2500$ K). Different interatomic potentials of W were tested, and the most appropriate one was selected by the thermodynamic and kinetic properties of W. Simulation results show that the dynamic migration of grain boundary can absorb the void, but the absorption efficiency of grain boundaries is sensitive to their structural characteristics, where the high-angle GBs are more absorptive to the void than the low-angle GBs. It is found that the void absorption cannot be completely attributed to the thermal diffusion mechanism during the GB-void interaction; the dynamic migration of high-angle GBs can significantly accelerate the void absorption. This study reveals a GB migration-induced self-healing mechanism of W at high temperatures.



Citation: Zheng, R.; Yang, L.; Zhang, L. Grain Boundary Migration as a Self-Healing Mechanism of Tungsten at High Temperature. *Metals* **2022**, *12*, 1491. <https://doi.org/10.3390/met12091491>

Academic Editors: Ayrat Nazarov and David Field

Received: 31 July 2022

Accepted: 7 September 2022

Published: 8 September 2022

Publisher's Note: MDPI stays neutral with regard to jurisdictional claims in published maps and institutional affiliations.



Copyright: © 2022 by the authors. Licensee MDPI, Basel, Switzerland. This article is an open access article distributed under the terms and conditions of the Creative Commons Attribution (CC BY) license (<https://creativecommons.org/licenses/by/4.0/>).

Keywords: molecular dynamics; tungsten; grain boundary; void

1. Introduction

Tungsten (W) is a prime candidate for use in plasma-facing components in fusion reactors. The high melting point of W can maintain its stable structural strength and performance at high temperatures, and the high thermal conductivity of W enables it to rapidly transfer the high temperature and heat generated by thousands of degrees Celsius in the nuclear fusion reaction. In addition, the low hydrogen retention of W can effectively reduce the performance degradation and even failure caused by various nuclear fusion particles remaining in the material. The main reason for the final performance failure of nuclear fusion components is that the material will produce a large number of point defects in its interior under the bombardment of fast-moving neutrons and other particles. Vacancies and interstitial atoms are the primary structural defects when energetic particles collide with materials [1]. These defects may subsequently evolve into microstructural flaws, such as voids, stacking fault tetrahedra (SFT), dislocation loops, etc. [2–6], leading to macroscopic degradation of the performance of the material [7]. The ability of a material to resist radiation damage is determined by how well the microstructure can remove vacancies, interstitial atoms, and their clusters. Much research has been devoted to understanding and controlling the behavior of structural defects to design materials that can withstand these harsh environments [8–13].

The introduction of interfaces into materials is an effective strategy and method to reduce irradiation damage [1–3]. It has been well confirmed that grain boundary (GB) can serve as defect sinks for absorbing and annihilating radiation-induced point defects. In

experiments, Chimi et al. [14] studied the effects of ion irradiation on nanocrystalline Au and showed that the irradiation-produced defects were thermally unstable because of the existence of a large volume fraction of GBs. Nita et al. [15] investigated the irradiation impact on the microstructure in nanostructured Ni and Cu specimens. They found that GBs can be a major sink for the defects, resulting in a much lower density of structural defects than that in coarser-grained material. Using molecular dynamics (MD) simulation, Bai et al. [4] proposed a ‘recombination mechanism’ of GB under radiation, that is, GBs firstly capture the radiation-induced interstitial atoms after collision cascades, leaving the abundant vacancies in grain. Then, the excess interstitial atoms on the boundaries escape back to the lattice and combine with nearby vacancies, promoting the vacancy-interstitial recombination subsequently. Although the radiation-induced structural defects absorbed by GBs have been preliminarily recognized, the understanding of how defects interact with GB at the atomic scale is still progressing [16,17]. In particular, while GB can provide a large energetic driving force for self-interstitial atoms (SIAs) to segregate to the GB, the radiation-induced vacancies and their clusters (e.g., voids) usually show less mobility than the SIAs. How GBs absorb structural defects with poor mobility needs further investigation.

The high-temperature environment generated by nuclear fusion reaction easily induces the changes in material microstructure, such as the grain growth induced by high temperature, which is essentially caused by the temperature-driven GB migration mechanism [18,19]. Therefore, understanding the interaction between the irradiation-induced structural defects and the dynamic moving GBs is significant in understanding the physical mechanism of interface defect elimination. However, different types of GBs have considerable differences in structure and properties, so they have different annihilation capacities and efficiency for irradiation-induced defects. In this paper, MD simulations were carried out to study the dynamic interaction between GBs and void to investigate the effect of different types of GBs on irradiation damage elimination, and a self-healing mechanism of the structural defects based on GB migration was proposed.

2. Methodology

The simulations were carried out on a bicrystal model using the parallel molecular dynamics code LAMMPS [20] with the embedded-atom method (EAM) interatomic potential for W. There are many kinds of interatomic potentials developed for a certain element, and no potential can fully and accurately reflect the physical parameters of a particular element. For example, some potentials are developed mainly to study the melting and solidification properties of a material, while others are developed to study its mechanical properties and deformation mechanisms. By the first screening of the potential database, four candidate EAM potentials developed for W were selected for further testing. The first potential (P1) [21] was developed for large-scale atomistic simulations in the ternary W–H–He system, focusing on applications in the fusion research domain. Following available ab initio data, the potential reproduces key interactions between H, He, and point defects in W and utilizes the most recent potential for matrix W. The second potential (P2) [22] was used to study the point defect properties of W. The parametrizations of the potentials ensure that the third-order elastic constants are continuous and have been fitted to the cohesive energies, the lattice constants, the unrelaxed vacancy formation energies, and the second-order elastic constants. The third potential (P3) [23] was developed for studying radiation defects and dislocations in W. This potential was fitted to a mixed database, containing various experimentally measured properties of W and ab initio formation energies of defects, as well as ab initio interatomic forces computed for random liquid configurations. The fourth potential (P4) [24] was developed to predict the behavior of point defects in body-centered cubic (BCC) metals, particularly interstitial defects, which is central to accurate modeling of the microstructural evolution in environments with high radiation fluxes.

The bicrystal model was used which enables us to explore individual GB characteristics and their effect on the interaction with crystal defects. The dimensions of each constructed bicrystal model were approximately $162 \text{ \AA} \times 204 \text{ \AA} \times 64 \text{ \AA}$ ($X \times Y \times Z$), and the total

number of atoms was about 1.3×10^5 . The GB was located at the intersection of grain A and grain B, and a void was placed in grain B, as shown in Figure 1a. Four symmetric tilt GBs are investigated in this study, namely $\Sigma 25(710)$ ($\theta = 16.3^\circ$) GB, $\Sigma 13(510)$ ($\theta = 22.6^\circ$) GB, $\Sigma 5(310)$ ($\theta = 36.9^\circ$) GB, and $\Sigma 29(520)$ ($\theta = 43.6^\circ$) GB. Different from the general definition of low-angle GB with misorientation angle $\theta < 15^\circ$, we distinguish high-angle and low-angle GBs from their structural properties, that is, the low-angle GBs are understood as a series of discrete dislocations. Therefore, we tentatively defined the $\Sigma 25$ and $\Sigma 13$ GBs as the low-angle GBs, and the $\Sigma 5$ and $\Sigma 29$ GBs were regarded as the high-angle ones in this study. The detailed GB structures are shown in Figure 1b where all the GBs contain topologically identical structural units, as outlined by the yellow line. They differ only by the distance separating the structural units and by their positions relative to the GB plane. In particular, the structure of the two low-angle GBs can be described as an array of discrete perfect dislocations, and the dislocation cores are formed by the structural unit. The voids were generated by removing atoms in a spherical region in grain B, and the void size was 10 \AA in this study.

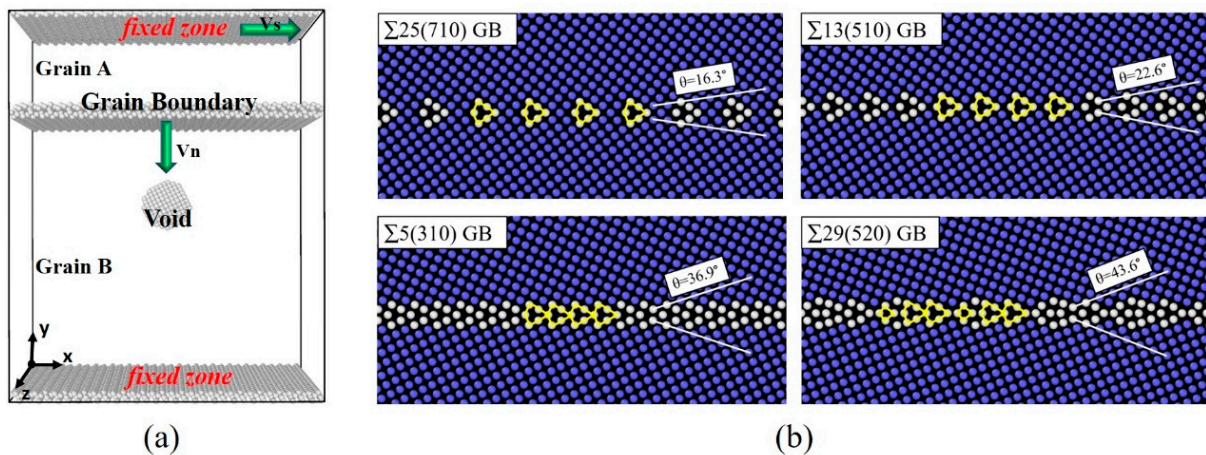


Figure 1. (a) Schematic of the bicrystal model used for simulations. (b) Atomic images of the equilibrium structure of $\Sigma 25(710)$ ($\theta = 16.3^\circ$) GB, $\Sigma 13(510)$ ($\theta = 22.6^\circ$) GB, $\Sigma 5(310)$ ($\theta = 36.9^\circ$) GB, and $\Sigma 29(520)$ ($\theta = 43.6^\circ$) GB. The GB structures are colored according to the common neighbor analysis (CNA) parameter. The structural units are outlined by the yellow lines.

To simulate the dynamic interaction between GB and the void, a constant shear velocity parallel to the boundary plane was applied to the bicrystal model to initiate GB motion. In particular, the shear strain was applied along the positive X -axis for $\Sigma 5(310)$ and $\Sigma 29(520)$ GBs, and along the negative X -axis for $\Sigma 25(710)$ and $\Sigma 13(510)$ GBs to guarantee the GB migration downwards. The periodic boundary condition was applied in the X and Z directions while a non-periodic boundary condition was applied in the Y direction. The atoms on the top of grain A and the atoms at the bottom of grain B were fixed. The thickness of each fixed slab was approximate twice the cutoff radius of atomic interactions while all the other atoms in the model were set free. The shear velocity was set as $V_s = 1 \text{ m/s}$ throughout the simulation, and the time increment of simulations was fixed at 2 fs . It is necessary to emphasize that the high shear velocity used in this study is due to the time-scale limitation of MD simulation, we employ the shear-induced GB migration to simulate the spontaneous GB migration at high temperatures in the real materials. The simulation temperatures were set as 2500 K , 3000 K , and 3500 K . Below this temperature range, the effect of GBs on void absorption is not obvious, and even void could hinder the movement of GBs, which is not within the scope of discussion in this study.

3. Results and Discussion

This study is mainly carried out in the high-temperature region (near the melting point) of W , the simulation results of each interatomic potential on the solid-liquid phase change

of W are tested first. A single crystal model of W with BCC structure was constructed. Before the heating process, the model was relaxed to an equilibrium configuration at 1000 K in the canonical ensemble NVT (constant atom number, constant box volume, and constant temperature). Then, the temperature gradually increases from 1000 K to 6500 K in the isothermal-isobaric ensemble NPT (constant atom number, constant pressure, and constant temperature). The total volume of the model was monitored during the heating process, as shown in Figure 2. The inserted snapshots show the atomic configurations of the single crystal model at different temperature levels. It was found that the BCC phase of the model has not changed much below 3000 K. After that, the disordered atoms (white atoms) increased considerably. The first-order phase transition (solid to liquid phase) was observed at about 5100 K for P1~P3, and 6000 K for P4, where the sample volume shows a sudden jump, as indicated by the red dotted lines. Obviously, the simulation result of P4 has a large deviation compared with the other three potentials. It is worth noting that the melting temperature of W simulated by MD is higher than that of the actual material, which is also a common phenomenon in other materials by MD simulation.

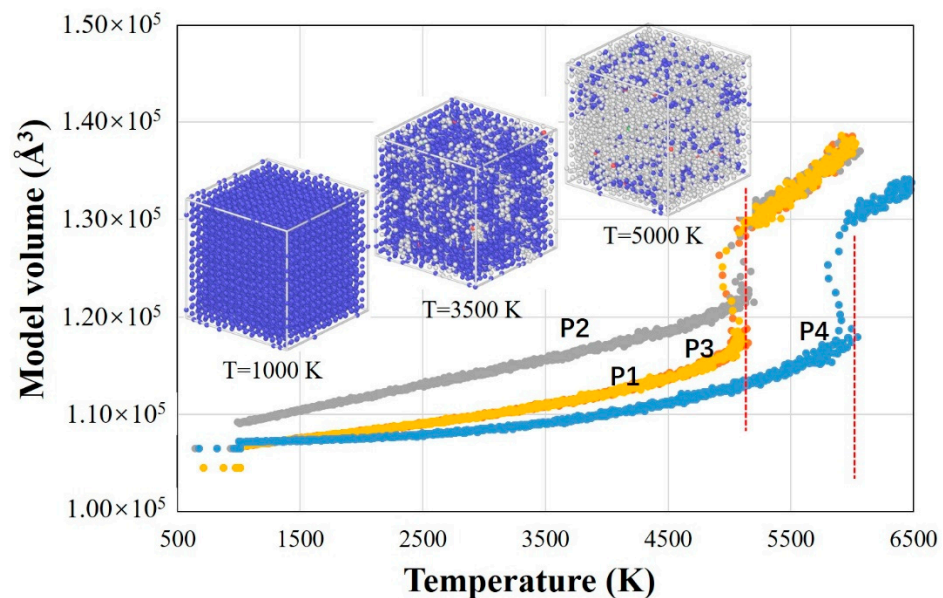


Figure 2. Model volume as a function of temperature simulated by four interatomic potentials. The inserted images are the atomic configuration of the model at different temperatures by P2. Atoms are colored by CNA method, where the blue atoms are in BCC structure, and the white atoms are in disordered structure.

To initiate the dynamic interaction between GBs and void, either void migrates towards the boundary or the dynamic moving of the boundary towards the void. Previous simulations have shown that the GB segregation energy of vacancy is much higher than the interstitial atoms, thus larger resistance must be overcome for the vacancy to move towards the boundary [25]. In addition, as the size of the vacancies cluster increases, the spontaneous movement of the cluster toward the boundary becomes more difficult [26]. At the MD simulation timescale, it is not easy to realize the void migrates towards GB. On the other hand, it was reported that the dynamic migration of various GBs can be achieved under shear deformation [27,28]. Therefore, the responses of GB under shear strain using the four potentials (P1~P4) are tested, as shown in Figure 3, where the $\Sigma 5(310)$ GB was selected as an example. For P1 and P3, a small section of GB migrated upwards under shear deformation, as indicated by the yellow box, and cracks initiated and expanded at the boundary plane with the increasing shear strain. For P2, when the critical shear stress was achieved, the whole boundary plane migrated downwards without producing any other structural defects. For P4, the boundary plane does not move under shear strain, but the structural transition from BCC to FCC occurred near GB when the shear stress achieved

a critical value. Based on the above simulations, P2 can best describe the thermodynamic and kinetic properties of W so it was selected as the interatomic potential to perform the subsequent simulations.

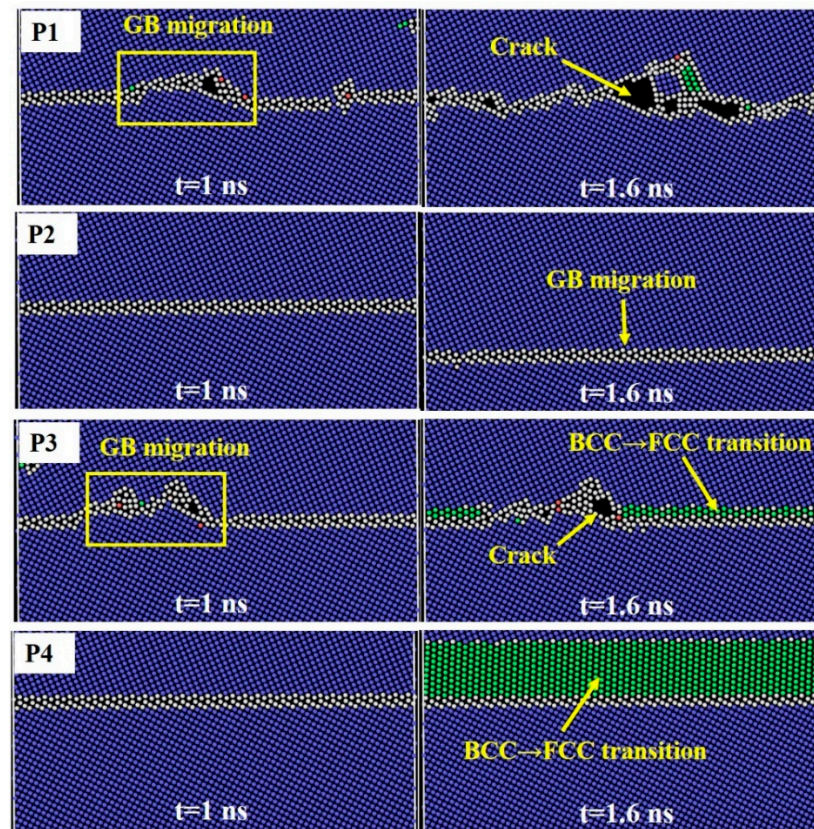


Figure 3. Atomic configuration of $\Sigma 5(310)$ GB under shear deformation at different simulation times using four interatomic potentials.

The simulation results show that the stress-driven GB motion occurred in all studied cases with P2. In specific, the system stress built up until it reached a critical value, and the GB jumped upwards abruptly from its original place to the next equilibrium position, accompanied by the release of local stress. The GB was kept stationary until the accumulated stress was large enough to trigger the next jump of GB. The periodic process keeps driving the motion of the boundary, leading to the GB migration downwards. It is worth noting that the GB migration velocity decreases with the increase in the misorientation angle of the bicrystal, that is, the $\Sigma 25(710)$ GB has the highest migration velocity while the $\Sigma 29(520)$ GB migrates the slowest. The dynamic migration of the four GBs and the process of their interaction with the void at a temperature of 3000 K are shown in Supplementary Videos S1–S4. In the videos, to clearly show the interaction between GBs and the void, the cross-sectional view of the void was presented by extracting the continuous four layers of atoms along the Z direction near the center of the void.

The migrating GB swept up the void in grain B as it passed by, and some different interactions have been observed depending on the GB characteristics. Figure 4 shows the snapshots of interactions between GBs and the preexisting void for $\Sigma 5(310)$ GB and $\Sigma 29(520)$ GB at 2500 K and 3000 K, respectively. The extracted profile of structural defects was presented via the visualization tool OVITO [29] using the dislocation extraction algorithm [30]. For $\Sigma 5(310)$ GB, after the interaction GB-Void interaction at 2500 K, the void remains there although it moves a certain distance from its original position due to the shear strain, and it was found the void was smaller in size compared with the original one, as shown in Figure 4(a1,a2). The result indicates that some vacancies were absorbed by the boundary after the interaction between GB and the Void. When the temperature

was increased to 3000 K, The void annihilated gradually into the boundary plane as the GB migration progressed, and it was eventually absorbed by the GB, leaving behind a defect-free area, as shown in Figure 4(a3). A similar scenario was observed for $\Sigma 29(520)$ GB. The size of the void was significantly reduced after the interaction, as indicated by the yellow arrow in Figure 4(b2). The smaller void size compared with that in Figure 4(a2) implies that $\Sigma 29(520)$ GB can absorb the vacancies more efficiently than $\Sigma 5(310)$ GB. The void was completely absorbed by the migrating boundary plane at the temperature of 3000 K, as shown in Figure 4(b3).

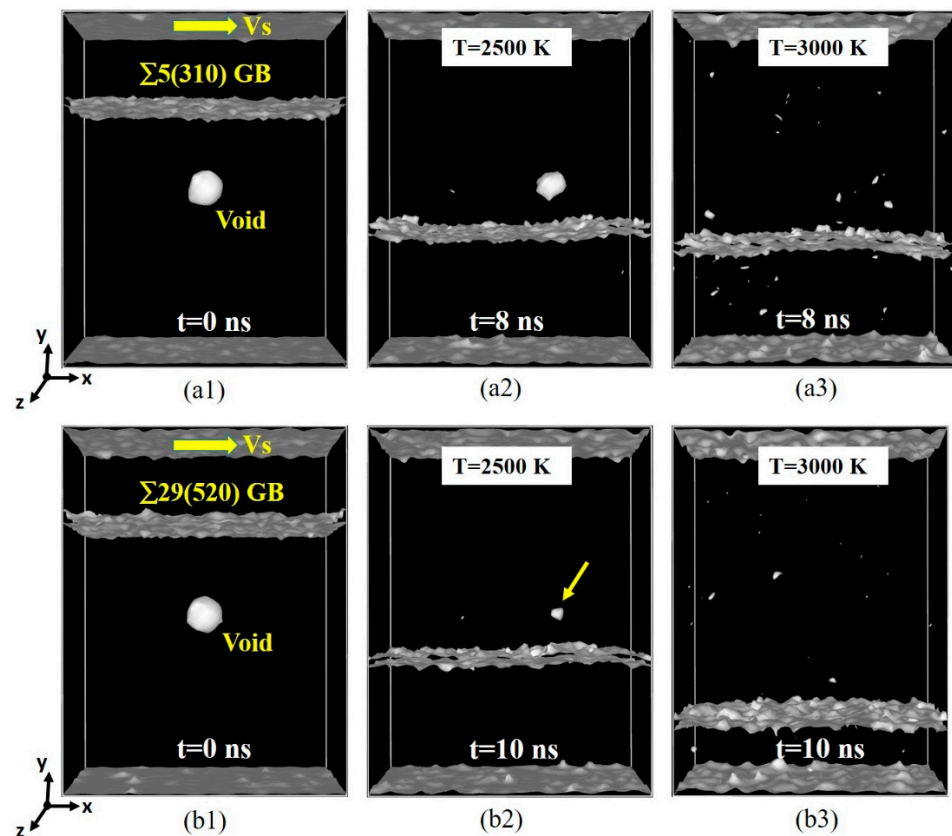


Figure 4. Snapshots of the interaction between GB and void at 2500 K and 3000 K. (a1–a3) $\Sigma 5(310)$ GB, (b1–b3) $\Sigma 29(520)$ GB. The extracted profile of GB and void was presented using the dislocation extraction algorithm. The dynamic process of GB-void interaction at 3000 K is shown in Supplementary Videos S1 and S2.

The interactions between the two low-angle GBs and the void are shown in Figure 5. As mentioned above, the low-angle GB can be regarded as consisting of a set of discrete dislocations, as indicated by the pink lines using the dislocation extraction algorithm. Different from the high-angle GBs, the size of the void has not changed significantly for the low-angle GBs after their interaction with the migrating GB at 3000 K, as shown in Figure 5(a2,b2). In the case of $\Sigma 25(710)$ GB, the void remains there after its interaction with the migrating GB even though the simulation temperature was increased to 3500 K, although the size of the void was further reduced (see Figure 5(a3)). In contrast, the void disappeared after the GB crossed over the void at 3500 K for the $\Sigma 13(510)$ GB. In a visual inspection of the simulation result, the high density of discrete dislocations was found to be connected to neighboring dislocations, which is due to the strong thermal diffusion mechanism of the GB atoms at high temperature, giving $\Sigma 13(510)$ GB the structural characteristics of high-angle GB, as shown in Figure 5(b3).

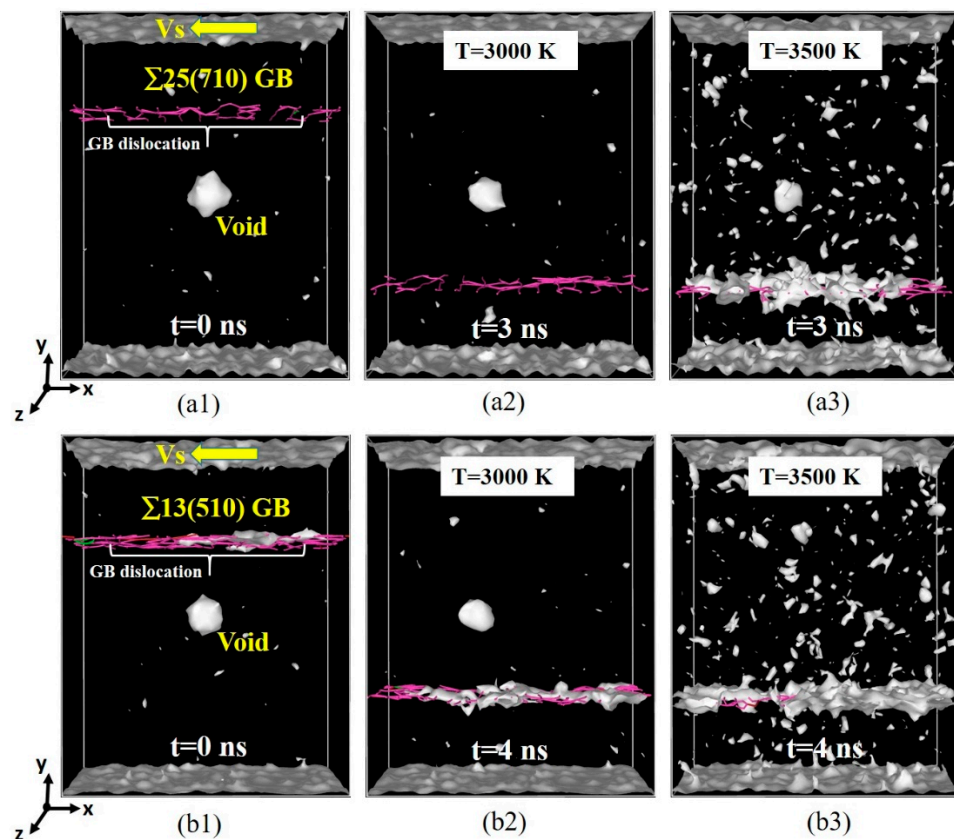


Figure 5. Snapshots of the interaction between GB and a void at 3000 K and 3500 K. (a1–a3) $\Sigma 25(710)$ GB, (b1–b3) $\Sigma 13(510)$ GB. The extracted profile of GB and void was presented using the dislocation extraction algorithm. The dynamic process of GB-void interaction at 3000 K is shown in Supplementary Videos S3 and S4.

According to the above simulation results, the following two aspects of information can be obtained. On the one hand, the high-angle GB has a strong ability to annihilate the void, while the low-angle GB has a relatively weak or even insignificant absorption efficiency for the void. This finding qualitatively agrees with the experimental results where the increased radiation tolerance was reported in the nanostructured materials that possess a large proportion of high-angle GBs [2]. The difference in void absorption efficiency between large-angle and low-angle GBs can be attributed to the size of the contact area between GB and void, which can be understood by the density of the structural units that consist of GB. As in Figure 1, the high-angle GBs are composed of continuous structural units, so that GB can fully contact the voids. In contrast, for a given size of void, the size of the contact area between low-angle GB and void is significantly reduced due to its discrete structural characteristic. Particularly, for low-angle GBs, the boundary with lower orientation has higher structural dispersion, which results in a smaller contact area between GB and voids, thus reducing the efficiency of the GB for void absorption. On the other hand, the simulations show that the increased temperature can facilitate the dissolution of the voids at GB. The effect of void size and temperature on the result of GB-void interaction has a close relationship with the thermal diffusion mechanism. The increased temperature enhanced the diffusion of atoms at GB (GB diffusion) as well as the thermal instability on the void surface in the grain (lattice diffusion), leading to the faster dissolution of the void at the higher temperature.

GB diffusion is profoundly different from lattice diffusion, and atoms in GBs are known to be much more mobile than in the lattice. It is reported that the difference between the diffusion coefficients of lattice diffusion and GB diffusion is about 10 orders of magnitude at about half of the melting temperature [31]. At the current timescale of MD

simulation, lattice diffusion is negligible compared to GB diffusion. Although there are considerable differences in diffusion coefficients within grains and at GBs, it was found that void absorption cannot be fully attributed to the thermally induced GB diffusion mechanism [32]. According to the simulations in this study, GB migration also plays an important role in void absorption. To explore the effect of the dynamic interaction between GB and the void, we further investigated the thermal stability of a void in the stationary GBs and the moving GBs. The mean-squared displacement (MSD) of atoms within the GB-void core region was computed. The core region is defined as 30 Å along the Y-axis within the boundary plane at the center. Figure 6 shows the MSD value as a function of the simulation time of different GBs during dynamic moving, and the MSD value of the four stationary GBs is inserted for comparison. The two high-angle GBs are computed at the temperature of 2500 K and 3000 K, while the two low-angle GBs are computed at 3000 K and 3500 K, respectively. For the stationary GBs, the calculated MSD values show that the difference in diffusion rate caused by the change in temperature is negligible. Obviously, it cannot explain the higher void absorption efficiency of the high-angle GBs. However, it was found that the calculated MSD values of the two high-angle GBs are much higher than that of the two low-angle GBs in the time region of the dynamic GB-void interaction, which is the main reason for the faster dissolution of the void at high-angle GBs. In addition, it can be found that the dynamic diffusion rate of the low-angle GBs is less sensitive than that of the high-angle GBs at high temperatures.

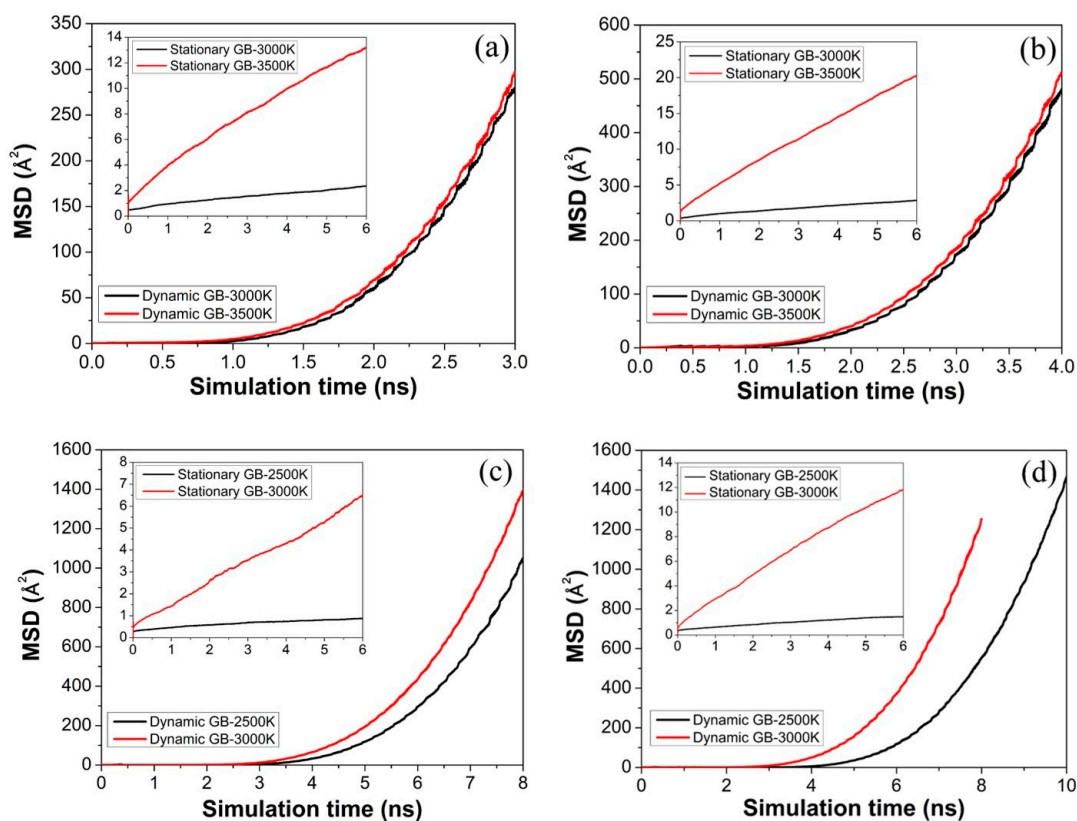


Figure 6. The mean-squared displacement (MSD) value as a function of the simulation time of different GBs during dynamic moving: (a) $\Sigma 25(710)$ GB; (b) $\Sigma 13(510)$ GB; (c) $\Sigma 5(310)$ GB; and (d) $\Sigma 29(520)$ GB. The inserted figures show the MSD value of the GBs at a stationary state.

To highlight the effect of GB migration in accelerating void absorption, the atomistic view of the void absorption in stationary and dynamic GBs is compared. Figure 7 shows the selected steps of the interaction between the void and the two high-angle GBs at 3000 K. To clearly show the interaction process between GB and voids, the cross-sectional view of the void was presented by extracting the continuous four layers of atoms along Z direction

near the center of the void. In Figure 7a, the void was placed at the center of the stationary $\Sigma 5(310)$ GB. The size of the void decreased gradually as the simulation time. At $t = 3$ ns, the void size is significantly reduced compared with the initial void, although it is not completely absorbed by the boundary plane. In Figure 7b, the $\Sigma 5(310)$ GB is above the void and it moved downward under the shear strain. When the dynamic GB moved close to the void, we began to record the change of the void with time. It was found that the void shrinks rapidly once it contacts with the GB, the void size reduced significantly after 1 ns and it was absorbed completely by the migrating GB after 1.2 ns. A similar process was observed in the simulation case of $\Sigma 29(520)$ GB. The void disappeared after 1.4 ns of the interaction between the migrating GB and the void. These results again indicate that GB migration can effectively accelerate void absorption.

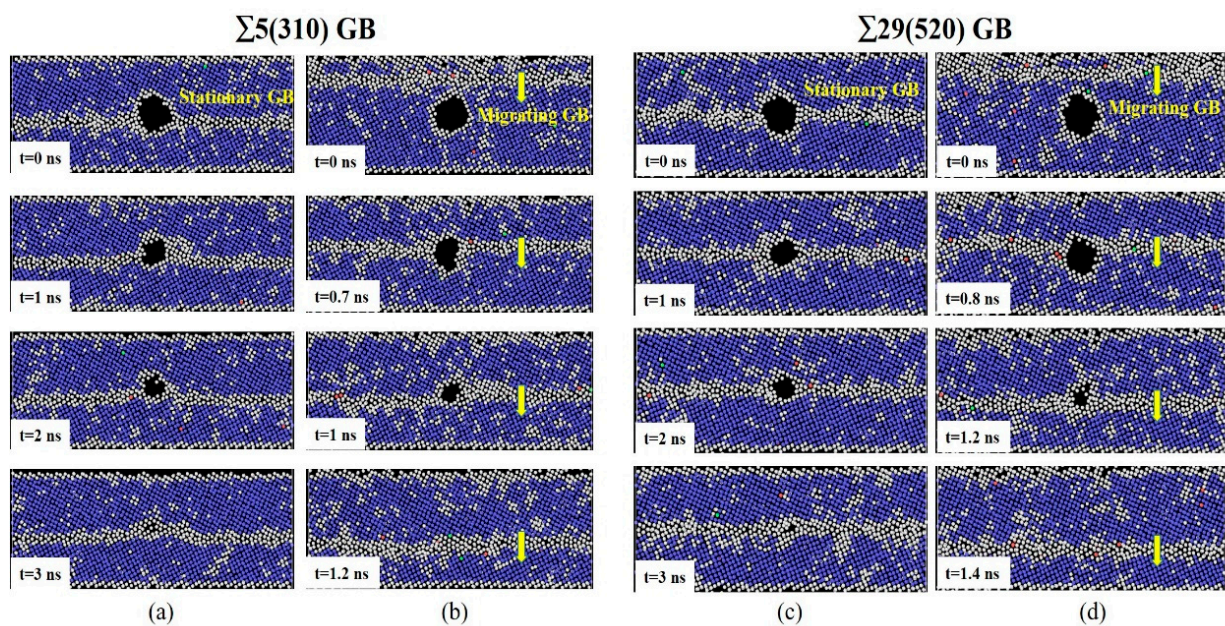


Figure 7. Cross-sectional view of the interaction between void and high-angle GBs: (a) stationary $\Sigma 5(310)$ GB; (b) dynamic $\Sigma 5(310)$ GB; (c) stationary $\Sigma 29(520)$ GB; (d) dynamic $\Sigma 29(520)$ GB.

4. Conclusions

MD simulations were carried out in this study to investigate the dynamic interaction between voids and migrating GB in bicrystal W at high temperatures of 2500 K to 3500 K. It was found that GB structure has a significant effect on the absorption of the void. The absorption efficiency of low-angle GBs is obviously lower than that of high-angle GB, although the increase in temperature can improve the absorption rate of low-angle GBs. The difference can be ascribed to the discrete GB structure and the fast GB migration velocity of the low-angle GB. By studying the diffusion rate of a void in the stationary GB and moving GB, we have shown that the absorption of the void at a migrating GB cannot be attributed solely to the thermal diffusion mechanism. The dynamic GB migration can substantially accelerate the absorption of the voids, revealing a GB migration-induced self-healing mechanism of W at high temperatures.

Supplementary Materials: The following supporting information can be downloaded at: <https://www.mdpi.com/article/10.3390/met12091491/s1>, Video S1: $\Sigma 5(310)$ GB. Video S2: $\Sigma 29(520)$ GB. Video S3: $\Sigma 25(710)$ GB. Video S4: $\Sigma 13(510)$ GB.

Author Contributions: Conceptualization, L.Z.; methodology, R.Z. and L.Z.; formal analysis, R.Z., L.Y. and L.Z.; resources, L.Z.; writing—original draft preparation, R.Z. and L.Y.; writing—review and editing, L.Z.; supervision, L.Z.; funding acquisition, L.Z. All authors have read and agreed to the published version of the manuscript.

Funding: National Natural Science Foundation of China (52071034; 52130107) and the Fundamental Research Funds for the Central Universities (2022CDJJKYJHJ005).

Institutional Review Board Statement: Not applicable.

Informed Consent Statement: Not applicable.

Data Availability Statement: The data required to reproduce these findings are available from the corresponding authors upon reasonable request.

Conflicts of Interest: The authors declare no conflict of interest.

References

1. Zhang, X.; Hattar, K.; Chen, Y.; Shao, L.; Li, J.; Sun, C.; Yu, K.; Li, N.; Taheri, M.L.; Wang, H.; et al. Radiation damage in nanostructured materials. *Prog. Mater. Sci.* **2018**, *96*, 217–321. [[CrossRef](#)]
2. Grimes, R.W.; Konings, R.J.M.; Edwards, L. Greater tolerance for nuclear materials. *Nat. Mater.* **2008**, *7*, 683–685. [[CrossRef](#)] [[PubMed](#)]
3. Ackland, G. Controlling Radiation Damage. *Science* **2010**, *327*, 1587–1588. [[CrossRef](#)]
4. Bai, X.M.; Voter, A.F.; Hoagland, R.G.; Nastasi, M.; Uberuaga, B.P. Efficient annealing of radiation damage near grain boundaries via interstitial emission. *Science* **2010**, *327*, 1631–1634. [[CrossRef](#)] [[PubMed](#)]
5. Kuksenko, V.; Pareige, C.; Pareige, P. Intra granular precipitation and grain boundary segregation under neutron irradiation in a low purity Fe-Cr based alloy. *J. Nucl. Mater.* **2012**, *425*, 125–129. [[CrossRef](#)]
6. Zhang, L.; Lu, C.; Tieu, K.; Su, L.; Zhao, X.; Pei, L. Stacking fault tetrahedron induced plasticity in copper single crystal. *Mater. Sci. Eng. A* **2017**, *680*, 27–38. [[CrossRef](#)]
7. Wirth, B.D. How does radiation damage materials? *Science* **2007**, *318*, 923–924. [[CrossRef](#)]
8. Griffiths, M. A review of microstructure evolution in zirconium alloys during irradiation. *J. Nucl. Mater.* **1988**, *159*, 190–218. [[CrossRef](#)]
9. El-Genk, M.S.; Tournier, J.-M. A review of refractory metal alloys and mechanically alloyed-oxide dispersion strengthened steels for space nuclear power systems. *J. Nucl. Mater.* **2005**, *340*, 93–112. [[CrossRef](#)]
10. Zhang, X.; Fu, E.G.; Misra, A.; Demkowicz, M.J. Interface-enabled defect reduction in He ion irradiated metallic multilayers. *JOM* **2010**, *62*, 75–78. [[CrossRef](#)]
11. Demkowicz, M.J.; Misra, A.; Caro, A. The role of interface structure in controlling high helium concentrations. *Curr. Opin. Solid State Mater. Sci.* **2012**, *16*, 101–108. [[CrossRef](#)]
12. Heinisch, H.L.; Gao, F.; Kurtz, R.J. The effects of interfaces on radiation damage production in layered metal composites. *J. Nucl. Mater.* **2004**, *329–333*, 924–928. [[CrossRef](#)]
13. Zhang, L. Understanding the Radiation Resistance Mechanisms of Nanocrystalline Metals from Atomistic Simulation. *Metals* **2021**, *11*, 1875. [[CrossRef](#)]
14. Chimi, Y.; Iwase, A.; Ishikawa, N.; Kobiyama, M.; Inami, T.; Okuda, S. Accumulation and recovery of defects in ion-irradiated nanocrystalline gold. *J. Nucl. Mater.* **2001**, *297*, 355–357. [[CrossRef](#)]
15. Nita, N.; Schaeublin, R.; Victoria, M. Impact of irradiation on the microstructure of nanocrystalline materials. *J. Nucl. Mater.* **2004**, *329–333*, 953–957. [[CrossRef](#)]
16. Bai, X.-M.; Uberuaga, B.P. The influence of grain boundaries on radiation-induced point defect production in materials: A review of atomistic studies. *JOM* **2013**, *65*, 360–373. [[CrossRef](#)]
17. Beyerlein, I.J.; Demkowicz, M.J.; Misra, A.; Uberuaga, B.P. Defect-interface interactions. *Prog. Mater. Sci.* **2015**, *74*, 125–210. [[CrossRef](#)]
18. Li, Y.H.; Wang, L.; Li, B.; Eisenstein, J.; Zhao, F.P.; Zhu, J.; Luo, S.N. Thermally driven grain boundary migration and melting in Cu. *J. Chem. Phys.* **2015**, *142*, 054706. [[CrossRef](#)]
19. Chen, K.; Han, J.; Srolovitz, D.J. On the temperature dependence of grain boundary mobility. *Acta Mater.* **2020**, *194*, 412–421. [[CrossRef](#)]
20. Plimpton, S. Fast Parallel Algorithms for Short-Range Molecular Dynamics. *J. Comput. Phys.* **1995**, *117*, 1–19. [[CrossRef](#)]
21. Bonny, G.; Grigorev, P.; Terentyev, D. On the binding of nanometric hydrogen-helium clusters in tungsten. *J. Phys. Condens. Matter* **2014**, *26*, 485001. [[CrossRef](#)] [[PubMed](#)]
22. Olsson, P.A.T. Semi-empirical atomistic study of point defect properties in BCC transition metals. *Comput. Mater. Sci.* **2009**, *47*, 135–145. [[CrossRef](#)]
23. Marinica, M.-C.; Ventelon, L.; Gilbert, M.R.; Proville, L.; Dudarev, S.L.; Marian, J.; Bencteux, G.; Willaime, F. Interatomic potentials for modelling radiation defects and dislocations in tungsten. *J. Phys. Condens. Matter* **2013**, *25*, 395502. [[CrossRef](#)] [[PubMed](#)]
24. Han, S.; Zepeda-Ruiz, L.A.; Ackland, G.J.; Car, R.; Srolovitz, D.J. Interatomic potential for vanadium suitable for radiation damage simulations. *J. Appl. Phys.* **2003**, *93*, 3328–3335. [[CrossRef](#)]
25. Tschopp, M.A.; Solanki, K.N.; Gao, F.; Sun, X.; Khaleel, M.A.; Horstemeyer, M.F. Probing grain boundary sink strength at the nanoscale: Energetics and length scales of vacancy and interstitial absorption by grain boundaries in α -Fe. *Phys. Rev. B* **2012**, *85*, 064108. [[CrossRef](#)]

26. Martinez, E.; Uberuaga, B.P. Mobility and coalescence of stacking fault tetrahedra in Cu. *Sci. Rep.* **2015**, *5*, 9084. [[CrossRef](#)]
27. Zhang, L.; Lu, C.; Michal, G.; Tieu, K.; Zhao, X.; Deng, G. Influence of temperature and local structure on the shear-coupled grain boundary migration. *Phys. Status Solidi B* **2017**, *254*, 1600477. [[CrossRef](#)]
28. Zhang, L.; Lu, C.; Shibuta, Y. Shear response of grain boundaries with metastable structures by molecular dynamics simulations. *Model. Simul. Mater. Sci. Eng.* **2018**, *26*, 035008. [[CrossRef](#)]
29. Stukowski, A. Visualization and analysis of atomistic simulation data with OVITO—The Open Visualization Tool. *Model. Simul. Mater. Sci. Eng.* **2010**, *18*, 015012. [[CrossRef](#)]
30. Stukowski, A.; Albe, K. Dislocation detection algorithm for atomistic simulations. *Model. Simul. Mater. Sci. Eng.* **2010**, *18*, 025016. [[CrossRef](#)]
31. Suzuki, A.; Mishin, Y. Atomic mechanisms of grain boundary diffusion: Low versus high temperatures. *J. Mater. Sci.* **2005**, *40*, 3155–3161. [[CrossRef](#)]
32. Zhang, L.; Shibuta, Y.; Lu, C.; Huang, X. Interaction between nano-voids and migrating grain boundary by molecular dynamics simulation. *Acta Mater.* **2019**, *173*, 206–224. [[CrossRef](#)]